Applied Catalysis B: Environmental 136–137 (2013) 248–259

Contents lists available at SciVerse ScienceDirect

Applied Catalysis B: Environmental

journal homepage: www.elsevier.com/locate/apcatb

Investigation of the role of platinum oxide for the degradation of phenol under simulated solar irradiation

Harrison S. Kibombo[a,*], Chia-Ming Wu[a], Rui Peng[a], Jonas Baltrusaitis[b], Ranjit T. Koodali[a,*]

[a] Department of Chemistry, University of South Dakota, Vermillion, SD 57069, United States
[b] PhotoCatalytic Synthesis Group, University of Twente, The Netherlands

ARTICLE INFO

Article history:
Received 21 September 2012
Received in revised form
25 December 2012
Accepted 28 January 2013
Available online 16 February 2013

Keywords:
Platinum
Titania
Photocatalysis
Surface studies
Phenol degradation

ABSTRACT

We demonstrate that a desired oxidation state can be achieved by synthetic colloidal methods and the choice of characterization technique is crucial for determining the physicochemical properties that influence the photocatalytic activities. XPS studies showed that PtO_2 was realized in this study, and the resultant crystalline PtO_2–TiO_2 prepared by subsequent hydrothermal treatment demonstrated activity for phenol degradation under simulated solar light irradiation. Preformed platinum based TiO_2 ensures control over the oxidation state and the crystallite size of titania. The role of Pt_{ox} in the form of stable Pt^{4+} is elucidated as a mild recombination center, whereas the crystallite size of Pt in surfactant free Pt^0–TiO_2 appears to be the overriding factor for attaining enhanced photocatalytic performance.

1. Introduction

The efficacy of heterogeneous photocatalysts is fundamentally dependent on the life time and fate of photogenerated charge carriers. Several methods have been employed to minimize charge recombination in metal oxide semiconductors, and incorporation of precious metals such as Pd, Au, Rh, Ag, and Pt has been investigated extensively. These metals exhibit a high electron affinity for photo-excited electrons generated in the conduction band of the metal oxide on band gap excitation. A proximate interaction between the metal and the semiconductor is essential in creating a Schottky barrier, such that when a Fermi level equilibration is achieved, interfacial charge transfer processes to the metal are facilitated through the metal–semiconductor heterojunction [1–4]. Of the existing precious metals investigated, Pt has emerged as a vital component in facilitating photocatalytic reactions owing to enhanced photostability, tunable physicochemical properties, and large work function [5]. Pt affinity for electrons is postulated to prolong electron–hole pair separation, and therefore impede their recombination, and consequently enhance the transfer of electrons to O_2 physisorbed on the TiO_2 surface [6].

The size and dispersion of Pt nanoparticles on semiconductor photocatalysts has a significant effect on the photocatalytic activity of the resulting Pt-supported catalyst. It is thus imperative to develop synthetic routes for the production of uniformly dispersed Pt nanoparticles of optimal size and highly active valence states for their respective applications. A variety of different approaches have been developed for the preparation of metal nanoparticles, and of the liquid phase approaches; microemulsion template [7], deposition-precipitation [8], photochemical deposition [9], sol–gel formation [10], and reverse micelle [11] methods have been explored extensively. The use of expensive organometallic precursors for the prevention of agglomeration may be minimized by use of transfer and stabilizing agents, such as quaternary ammonium salts [12], citrate [13], organo-sulfates [14], phosphines [15], polyols [16], alkylamines [17], alkylthiols [18], synthetic [19], and natural polymers [20] during the particle synthesis process. Although these different preparative procedures could yield varying sizes of nanoparticles, it has been demonstrated that the control of size of the catalytic particles can be more easily achieved by surfactant stabilization. The control of size and distribution may be improved by direct synthesis of Pt nanoparticles in an organic phase or by the transfer of nanoparticles from aqueous to organic phase, owing to the low interfacial energies in the latter [21,22].

In addition to the size and dispersion, the valence state of noble metals supported on semiconductor photocatalysts is an important factor that needs to be ascertained in order to derive a

* Corresponding authors. Tel.: +1 605 677 6189; fax: +1 605 677 6397.
E-mail addresses: Harrison.Kibombo@usd.edu (H.S. Kibombo), Ranjit.Koodali@usd.edu, ktranjit@gmail.com (R.T. Koodali).

0926-3373/$ – see front matter © 2013 Elsevier B.V. All rights reserved.
http://dx.doi.org/10.1016/j.apcatb.2013.01.062

structure-activity relationship. In several instances, the oxidation states of Pt have not been fully characterized by XPS studies leading to some uncertainties in the interpretation of data since it well documented that Pt can interact with chemisorbed oxygen and form PtO and/or PtO_2 [23–29]. In these studies, the presence of Pt(0) has been inferred from TEM studies but as stated before, surface characterization has not been performed to verify if the oxidized forms of Pt are present. Furthermore, in cases where the oxidation states of Pt have been evaluated, the presence of PtO and/or PtO_2 have been discerned. In such systems, it is very difficult to ascertain the contributions of each of these valence states toward the resulting photocatalytic activity of the material without having a reference photocatalyst that contains Pt exclusively in one oxidation state, *i.e.* PtO/TiO_2 or PtO_2/TiO_2. In this study, we are able to compare the photocatalytic activity of TiO_2 with that of PtO_2/TiO_2 (with different loadings) and clearly understand the role of PtO_2 in photocatalytic reactions. For comparison purposes, we have also prepared $Pt/PtO_2/TiO_2$, and $PtO/PtO_2/TiO_2$, photocatalysts and the activities of these catalysts are reported in this manuscript.

We utilize the phase transfer reduction method where an aqueous solution of metal precursor (K_2PtCl_4,) is transferred into the organic (toluene) phase by means of tetra-*n*-octylammonium bromide (TOAB) that serves as both the phase transfer and capping agent. The metal is reduced by an aqueous solution of sodium borohydride ($NaBH_4$) in preference to other reductants such as alcohol [13], *N*,*N*-dimethylformamide [30], citrate, polyalcohol, *L*-ascorbic acid [31], and other approaches such sonochemical reduction [14], photoreduction [32], N_2 [33] and H_2 reduction [34]. Known amounts of the Pt nanoparticle solution were then added along with the titania precursor ($Ti(OPr^i)_4$) and subject to hydrothermal treatment followed by reduction in H_2. After hydrothermal reaction (in an oxidizing environment) and subsequent reduction, metallic platinum, Pt^0 could co-exist with Pt_{ox} as PtO and PtO_2 particles on the TiO_2 surface. Surprisingly, we observe that this method of preparation leads to the formation of PtO_2/TiO_2. However the role of PtO_2 dopants on photocatalytic oxidation of phenol has not been clearly elucidated, and needs to be clarified for aqueous phase photocatalytic reactions. PtO_2/TiO_2 showed higher activity than TiO_2 in gaseous CO oxidation but not for acetone oxidation [35]. Huang and co-workers evidenced that mixed valence states of PtO-PtO_2 were not only visible light sensitizers but also facilitated the oxidation of NO_2 to NO_3^- by suppression of NO_2 selectivity in the gas phase [36]. Wang and co-workers utilized photoluminescence spectroscopy to attribute the photocatalytic oxidation of NO in gas phase to the prolonged lifetime of electrons and holes in Pt_{ox} catalyst; whereas the dopants that existed as metallic Pt and platinum chloride exhibited negligible contribution [37]. On the contrary, Lee and Choi showed that Pt_{ox}/TiO_2 strongly inhibited the degradation of trichloroethylene and perchloroethylene but it was more reactive than TiO_2 for the degradation of dichloroacetate. It was also interesting to note that the oxidation state of Pt had minimal influence on the activity of phenolic compounds such as 4-chlorophenol [38].

The motivation for this work is to discern the role of the oxidation state of Pt on organic degradation considering the ambiguity regarding the efficacy of Pt_{ox}. We have used the degradation of phenol as a model reaction. The photocatalytic degradation of phenol over Pt/TiO_2 has been reported previously [24,28,39], but XPS studies were not reported in these papers to discern the oxidation state(s) of Pt. The preparation methods for Pt particles are crucial in determining the resultant oxidation state. *Tetra*-alkyl ammonium halides such as TOAB have used for the preparation of uniformly sized Pt nanoparticles. Although the role of the TOAB concentration on the preparation of Pt/C [22] and bimetallic Pt–Cu [40] has been studied, there is lack of evidence in the literature demonstrating the effect of the surfactant on the oxidation state of the metal on the supported catalyst. This is the first report detailing the synthesis of crystalline PtO_2–TiO_2 that demonstrates control over the oxidation state using TOAB, while eliminating the use of strong organic solvents such as THF [22] and strong reducing agents such as polyoxometalates [38]. The significance of full characterization is exemplified and the use of X-ray photoelectron spectroscopy (XPS) is emphasized to elucidate how synthetic methods influence the oxidation states of Pt, and thus subsequently modulate titania activity in the photo-oxidation of organic compounds such as phenol. Contrary to expectation, the oxidation states of Pt (as Pt^0, PtO, or PtO_2) are invariant during the photocatalytic reaction in our study. In addition, XPS studies have been carried out at various stages of preparation, *i.e.* freshly prepared (hydrothermal method), reduced (in hydrogen flow), calcined, and spent photocatalysts to understand the valence state of Pt and its influence on the photocatalytic activity toward degradation of phenol.

2. Experimental

2.1. Materials

The photocatalysts were prepared using the following commercially available chemicals sans further purification; ethanol (Pharmco-AAPER, A.C.S/USP grade, anhydrous), hydrogen hexachloroplatinate (IV) hydrate (H_2PtCl_6, Acros, ACS grade), titanium isopropoxide ($(Ti(OPr^i)_4$, $Ti[OCH(CH_3)_2]_4$, Acros, 98 + %), tetraethylorthosilicate (TEOS, $Si(OC_2H_5)_4$, Acros, 98%), potassium (II) tetrachloroplatinate (K_2PtCl_4, Pressure Chemical Co.), tetra-*n*-octylammonium bromide (TOAB, $[CH_3(CH_2)_7]_4N$ Br, Alfa Aesar, 98+%), sodium borohydride powder ($NaBH_4$, Acros, 98+%), 4-dimethyl-aminopydridine (DMAP, $(CH_3)_2NC_5H_4N$, Acros, 99%), toluene (Acros, ACS grade), and conc. nitric acid (HNO_3, Acros, ACS grade). Chromatographic analyses were carried out using deionized water (resistivity >18 MΩ-cm) solutions of appropriately diluted phenol (Acros, 99+%, ACS grade), hydroquinone (Sigma, >99%), 1,2,4-benzenetriol (Aldrich, 99%), pyrogallol (Alfa Aesar, 99% packed under argon, ACS grade), fumaric acid (Acros, 99+%), maleic acid (Alfa Aesar, 98+%), and methanol (Acros, 99.9% HPLC grade). In addition, benzoquinone (TCI America, 98%) was purified by sublimation to obtain bright yellow crystals, and collected prior to use.

2.2. Gel synthesis

A modified procedure based on Kibombo et al. [10] was adapted for the preparation of the platinized mesoporous gels. The sol–gel addition of precious metallized platinum complex solutions to the titania phase was achieved using two simple synthetic approaches that we conveniently refer to as direct template (DT) and direct infusion (DX) methods.

2.2.1. Synthesis of preformed Pt^0 nanoparticles

Prior to metal–semiconductor composite synthesis, preformed platinum metal nanoparticles were prepared. $[PtCl_4]^{2-}{}_{(aq)}$ ions capped with tetra-*n*-octylammonium bromide (TOAB) were prepared by a phase transfer method, and reduced by $NaBH_{4(aq)}$ to form preformed Pt^0 nanoparticles. TOAB in 40 mL of toluene (50 mM) was dissolved in an aqueous solution of 19.4 mL of 23.2 mM K_2PtCl_4, and stirred at 300 rpm for 1 h. The organic phase was dried with dropwise addition of 8–12 mL of freshly prepared 0.1 M $NaBH_{4(aq)}$. Stirring was continued overnight at 300 rpm prior to washing repeatedly with equal amounts (40 mL) of H_2O, 0.1 M H_2SO_4, and 0.1 M NaOH. The resultant organosol was dried with anhydrous Na_2SO_4 and the organic phase denoted as Pt-TOAB. These preformed platinum nanoparticles were used in the subsequent sol–gel reaction.

2.2.2. Synthesis of Pt/TiO_2 materials

For the DT method, portions of preformed Pt-TOAB corresponding to 0.5, 1, and 2 wt.% Pt were incorporated in separate Teflon liners. Hydrolysis of the titania precursor (2.2 mL of $Ti(OPr^i)_4$) was induced by addition of 1 mL of H_2O and catalyzed by 100 μL of conc. HNO_3. The suspensions were left to stir up to 3 h to enhance homogeneity and gelation.

Control experiments for each loading were carried out in the absence of stabilizing agents by simply incorporating hexachloroplatinate to the sol–gel route in place of the preformed platinum nanoparticles. The DX method constituted of slow infusion of 0.075, 0.15, and 0.30 mL of 0.2 M H_2PtCl_6 corresponding to the aforementioned percentage loadings in the gel respectively, in the presence of 18 mL of ethanol, 2.2 mL of $Ti(OPr^i)_4$, 1 mL of H_2O and 100 μL of conc. HNO_3 as described for the DT method.

The resultant gels from both methods were subjected to hydrothermal treatment in a Thermolyne autoclave reactor furnace, and heated to a temperature of 120 °C for 14 h. The gels or gelatinous precipitates attained were filtered, washed, and oven dried at ~70 °C overnight. The materials formed were carefully ground and calcined at 450 °C under H_2 flow for 6 h at a heating rate of 3 °C/min.

2.3. Structural characterization

Prior to the investigation of structural and textural properties, the calcined materials were dried overnight at ~70 °C. Powder X-ray diffraction (XRD) patterns were collected on a Rigaku Ultima IV at room temperature employing Ni filtered Cu Kα radiation (λ = 1.5408 Å), operated at an accelerating voltage of 40 kV, and emission current of 44 mA. The angle regions scanned were over a long range of 2θ = 20–80° with a step size of 0.02° and a scan speed of 1°/min to obtain information on phase composition. The TiO_2 crystallite sizes were determined using PDXL software. 2θ peaks at 48.0°, 62.7°, and 75.1° were used to estimate the titania crystallite sizes in all the samples. The uncertainty in the determination of the crystallite size is ±1 nm.

N_2 physisorption analyses were carried out after degassing the materials at 100 °C for at least 1 h. N_2 adsorption–desorption isotherms were then obtained at 77 K using Quantachrome Nova 2200*e* surface area and pore size analyzer. The surface areas were calculated by using the Brunauer–Emmett–Teller equation within a relative pressure range (P/P_0) of 0.05–0.30. The pore volume was determined from the amount of nitrogen adsorbed at the highest relative pressure of $P/P_0 \sim 0.99$. The pore diameter was determined by applying the Barrett–Joyner–Halenda (BJH) model to the desorption isotherm.

Diffuse reflectance (DR) spectra were recorded over the 200–600 nm range using a Cary 100 Bio UV–vis spectrophotometer equipped with a Harrick DR praying mantis accessory. The resultant spectra obtained were converted to Tauc plots *via* the Kubelka–Munk function in order to estimate the band gap energies of the photocatalysts. Further details on the morphology of the Pt and TiO_2 were attained by employing transmission electron microscopy (TEM), and the micrographs were obtained using a Tecnai G^2 instrument operating at accelerating voltage of 120 kV. The samples for TEM studies were prepared by dispersing Pt–TiO_2 in ethanol for 1 h by sonication. A drop of the suspension was cast on the 200 mesh copper grid coated with carbon type-B support film, and allowed to dry overnight in a petri dish prior to imaging.

The dispersion and average particle sizes of Pt were estimated by CO pulse chemisorption using CHEMBET-3000 TPR/TPD (Quantachrome Instruments) at ambient conditions. The materials and quartz U-tube were dried at ~70 °C overnight prior to analysis. An adsorbate and carrier gas flow of 90 mL/min and heating rate of 10 K/min were maintained throughout the course of the experiment. Typically, 90–100 mg of material was loaded into the U-tube, outgassed at 130 °C for 1 h under He flow, and then cooled to room temperature. After switching the gas to H_2 and stabilizing the flow, the material was reduced at 350 °C for 2 h, and cooled to room temperature again. The gas was switched back to He, and CO gas was introduced through the calibration titration valve. The thermal conductivity detector (TCD) signal was stabilized at an attenuation of 8 and detector current of 150.0 mA by using the coarse and fine adjustment knobs. CO pulses (100 μL each) were injected into the carrier gas until the pores of the material were saturated. The TCD response was due to the quantity of non-chemisorbed adsorbate. The platinum dispersion and particle size measurements were calculated using pulse titration analysis generated by Quantachrome TPRWin v2.1 software. The dispersion estimates are based on the ratio of Pt species accessible to the CO relative to the total number of Pt species present in the sample under investigation. Inductively Coupled Plasma Mass Spectrometry (ICP–MS) estimated that the amounts of Pt in the Pt–TiO_2 photocatalysts were within range of initial amount incorporated in the synthesis gel thus indicating good retention of the precious metal in the mesostructure.

The surface composition and oxidation state of platinum was investigated by using a custom-designed Kratos Axis Ultra X-ray photoelectron spectroscope, equipped with an Al Kα X-ray source of 1486 eV. Base pressure in the analysis chamber was 5×10^{-10} Torr. The X-ray gun was operated at an emission current and accelerating voltage of 15 mA and 15 kV respectively. Low-energy electrons were used for charge compensation, and subsequent neutralization of the sample. Survey scans were collected using the following instrument parameters: energy scan range of 1200 to 0 eV, step size of 1 eV, and X-ray spot size of 700 × 300 μm. High-resolution spectra were acquired in the region of interest using the following experimental parameters: 20–40 eV energy windows pass energy of 20 eV, step size of 0.1 eV, and a dwell time of 1000 ms. One sweep was used to obtain a survey spectrum of all binding regions. The absolute energy scale was calibrated to the C 1s peak binding energy of 284.6 eV. The $4f_{7/2}$ binding energies of Pt, PtO, and PtO_2 were constrained at 71.0 ± 0.1 eV, 73.0 ± 0.1 eV, and in the range 75.0 ± 0.1 eV respectively. In addition, the Pt 4f doublet ($4f_{7/2}$, $4f_{5/2}$) was separated into two peaks with an intensity ratio of 4:3, and an energy shift of 3.3 eV. All the peaks used for quantification were Gaussian/Lorentzian shape GL (30:70) curves with equivalent eV at the full-width-half-maximum (fwhm).

The effect of Pt loading on the charge separation efficiency in TiO_2 was detected by photoluminescence studies using a Flouromax-4 (JY Horiba) fluorometer. Each photocatalyst was finely ground in an appropriate amount of KBr, and then pressed into a pellet prior to light excitation at a wavelength of 382 nm. The emission spectra were monitored at 420 nm and the intensities were compared to estimate the extent of charge recombination in the photocatalysts.

2.4. Photocatalysis experiments using Pt–TiO_2 materials

The photocatalytic efficiencies of the Pt–TiO_2 materials were evaluated by monitoring the degradation of phenol from aqueous suspensions over a 2 h period. 100 mg of photocatalyst were suspended in 100 mL of 2×10^{-4} M phenol solution (initial pH of 4–5) in a quartz cylindrical jacket reactor, and stirred in the dark for 30 min at 300 rpm under O_2 purge (60 mL/min) to ensure that the adsorption–desorption equilibrium is reached.

The reaction temperature was kept constant under 30 °C by using a water circulation bath, and simulated solar irradiation was supplied using a Xenon lamp (Newport 1000 W) equipped with a 1.5 AM filter. The light intensity in the reaction medium was estimated to be 92 mW/cm^2 by placing the reactor 6 cm away from the light source. The intensity at back outer surface of reactor

(without suspension), I_s = 113 mW; intensity at back outer surface of reactor (with suspension) I_{os} = 9.28 mW; and intensity of light in reaction medium $I_r = (I_s - I_{os})/\pi r^2$ = 91.7 mW/cm^2. These conditions were maintained throughout the course of the experiment. 15 mL aliquots were collected every 30 min and each suspension was centrifuged at 3200 rpm for 15 min, filtered through a 0.45 μm Millipore filter membrane, and the clear solutions were analyzed for organic content as described in the subsequent sections of this manuscript. Experiments were carried out under N_2 flow (absence of oxygen) in order to investigate the role of catalysis on the Pt surface and the role of oxygen in the reaction medium. In addition, the contribution of hydroxyl radicals (•OH) on the photocatalytic reaction was studied by applying the fluorescence technique that detects the amount of •OH formed on illuminated TiO_2 and Pt–TiO_2 surfaces using terephthalic acid (TPA) as a chemical trap for the •OH radicals. These radicals are known to react readily with TPA to produce highly fluorescent 2-hydroxyterephthalic acid. 20 mg of photocatalyst were added to 50 mL of 5×10^{-4} M TPA solution in 2×10^{-3} M NaOH, prior to solar simulated irradiation. 3 mL aliquots were drawn every 20 min for a duration of 80 min, filtered through a 0.45 μm Millipore filter membrane, and analyzed using Flouromax-4 (JY Horiba) fluorometer. The fluorescence emission intensity of the 2-hydroxyterephthalic acid produced a peak at 425 nm after excitation at 315 nm. The intensity of the peak at 425 nm is expected to be proportional to the amount of •OH formed.

2.5. Degradation efficiencies of Pt–TiO_2 materials

The catalytic performance of the platinized titania materials was evaluated by estimating the amount of organics remaining in solution using a Shimadzu TOC-V CSH Total Organic Carbon (TOC) Analyzer immediately after filtration. Also post photocatalysis experiments, identification and quantification of unreacted phenol and its reaction intermediates was carried out by High Performance Liquid Chromatography (HPLC) using a Spectra-Physics 8800 chromatograph equipped with an Alltech Ultrasphere C-18, 5 μ long reverse phase column of 250 mm length, internal diameter of 4.6 mm, and a Spectra 100 Variable wavelength detector. The eluents constituted of a methanol/water mobile phase composition of 40:60 by volume (with 1 vol.% glacial acetic acid), flowing at a rate of 1 mL/min, and detected at a wavelength of 254 nm.

Stock solutions of desired concentrations of hydroquinone (HQ), phenol (PhOH), benzoquinone (BQ), fumaric acid (FA), pyrogallol (PG), catechol (CC), and 1,2,4-benzenetriol (HHQ) were prepared in deionized water for the identification of degraded intermediates of phenol. Calibrations plots were derived from the solutions diluted to concentrations in the range between 2×10^{-5} M and 2×10^{-4} M, and purged with argon to minimize autoxidation. We estimate the reproducibility of our photocatalytic experiments to be within 5%.

3. Results and discussion

3.1. Proposed mechanism for the formation of PtO_2

Pt-TOAB was prepared by a protocol derived from Brust et al. [41]. Scheme 1 illustrates the process through which preformed Pt (Pt-TOAB) was utilized to prepare PtO_2/TiO_2. K_2PtCl_4 was extracted from the aqueous phase to the organic phase (toluene) by using tetra-*n*-octylammonium bromide (TOAB) as the stabilizing agent to reduce the tendency of particles to grow and agglomerate. The transfer of Pt^{4+} ions is proposed to occur *via* electrostatic attraction between the positively charged TOA^+ ($[(C_8H_{17})_4N]^+$) ions and the negatively charged tetrachloroplatinate $[PtCl_4]^{2-}$ ions, and can be observed by a color change to yellow. These ionic interactions may impart hydrophobic properties (due to presence of phase transfer agent, TOAB) that facilitate efficient transfer of the Pt ions from the aqueous to organic phase [42]. After 40 min of stirring, the two phases were separated and the transfer of $[PtCl_4]^{2-}$ to the organic phase was evidenced by the deep brown color. The organic phase was subsequently dried over anhydrous Na_2SO_4. The dropwise addition of a few mL of 0.1 M $NaBH_4$ solution was intended to reduce the Pt species to their lowest oxidation state. A deepening in the color was observed, suggesting that the reduction of Pt^{2+} species was achieved. The UV–vis spectrum for diluted K_2PtCl_4 aqueous solution indicates a strong peak around 216 nm, with a shoulder at 227 nm, attributed to ligand-to-metal (LMCT) charge transfer from Cl^- to Pt^{2+} as illustrated in Fig. 1. The band at 216 nm may also be associated with a hydrolyzed product from the hydrolysis of K_2PtCl_4. After phase transfer, a strong peak at 288 nm due to $^1A_{1g}$–$^1T_{1u}$ d–d transitions was observed [32,43,44] and confirmed the presence of reduced Pt in the organic TOAB phase.

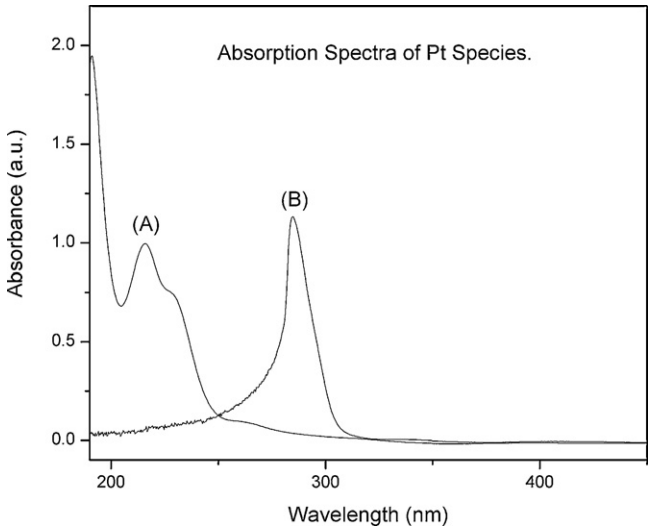

Fig. 1. UV–visible spectra of platinum species of diluted (A) K_2PtCl_4 in aqueous media and (B) Pt-TOAB in toluene (organic) media.

Pt-TOAB was further incorporated into the sol–gel route in the presence of ethanol in order to obtain the desired Pt loading. The synthesis is further accelerated by hydrothermal treatment to promote hydrolysis and achieve gelation. Specifically, we propose that this reaction condition is important in providing an environment that influences structural properties such as surface area, crystallinity, and the oxidation state that are often alluded to as significant factors for achieving high performance organic degradation photocatalysts.

3.2. Structural effects of platinum on TiO_2

Fig. 2 displays the high angle powder XRD patterns elaborating the structural features of the platinized TiO_2 materials. The diffractograms of the photocatalysts prepared in this study exhibit peaks at 2θ = 25.3°, 37.8°, 48.0°, 53.9°, 55.1°, 62.7°, 68.7°, 70.3°, 75.1°, and 76.0° due to d_{101}, d_{103}, d_{004}, d_{200}, d_{105}, d_{211}, d_{204}, d_{116}, d_{220}, d_{215}, and d_{301} respectively attributed to the anatase phase. A platinum loading of 0.5 wt.% by the DT method (use of Pt-TOAB) resulted in high intensity anatase peaks of sharp contrast as shown in Fig. 2A. The profiles of the DT derived photocatalysts of higher loading *i.e.* 1 and 2 wt. % are somewhat similar suggesting similar crystallinity and crystallite sizes of titania.

Control experiments for each loading were prepared to study the influence of the absence of capping agent on the structural properties. These materials were synthesized by the DX method and the XRD patterns are compared to those of the Pt-free

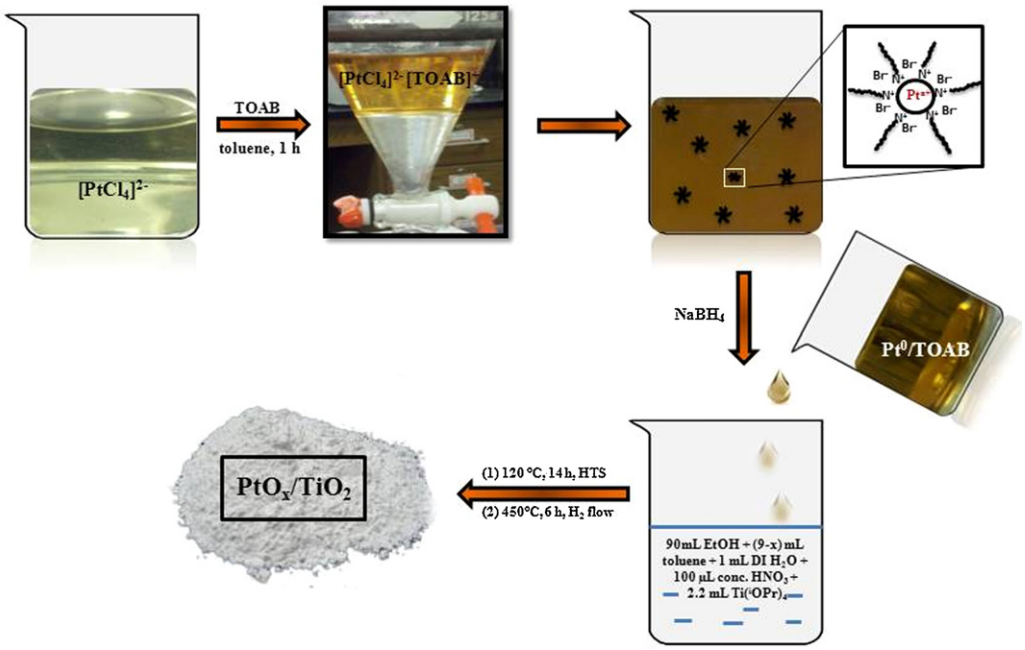

Scheme 1. Proposed mechanism for the preparation of PtO_2/TiO_2.

titania material as shown in Fig. 2B. The material containing 0.5 wt.% Pt exhibits peaks of higher intensity and sharper contrast than its counterparts. This is indicative of the crystallinity enhancement by using the DX method, and the formation of larger anatase crystallite sizes (14.7 nm) with fewer defects. Doubling the platinum amount (1 wt. %) resulted in a material displaying similar characteristics and no diffraction peaks due to platinum were observed suggesting improved dispersion of Pt species, and more homogeneity in the formation of Pt oxides. However, low intensity peaks observed at 39.7° and 46.4° due to Pt *d*-spacings of d_{111} and d_{200} emerged at a higher loading of 2 wt.%. With respect to the doublet at ~55°, an increase in Pt loading appears to be accompanied by a loss in diffraction contrast thus implying smaller crystallite sizes of titania. The distribution of these small particles in the mesostructure is relevant to the photocatalytic activity and thus the physisorption properties were investigated to provide information pertaining to the access of these active sites.

The nitrogen isotherms of the Pt–TiO_2 oxides prepared by the two synthesis methods were examined and the profiles are shown in Fig. 3. The oxides prepared by the DT method exhibit type IV isotherms suggesting the mesoporous nature of the pores as shown in Fig. 3A.

The materials prepared by surfactant free methods (DX) exhibit isotherms of type IV that is characteristic of mesoporous materials and appear to retain similar physisorption properties at low Pt loading of 0.5 and 1 wt.% as illustrated in Fig. 3B. An increment to 2 wt.% (DX2) results in a variation of the physisorption profile. At low relative pressures, the initial stretch of the type IV isotherm is ascribed to monolayer adsorption that gradually progresses to multilayer adsorption and culminates in capillary condensation. The Pt-free titania is shown for comparison and exhibits properties that are similar to DX2. The variation in pore geometries in such materials is evidenced by hysteresis that is a reflection of the mechanism through which physisorbed nitrogen molecules access to and from the pores. The pores of larger sizes may empty into their environment *via* smaller pores at pressures coinciding with capillary evaporation of the connecting cavities [45]. We observe that Pt–TiO_2 materials demonstrate H3 type hysteresis that does not level off at high relative pressures. Such occurrences are associated with materials composed of loose assemblies of irregular shaped plate-like particles of slit-like pore morphology [46]. These sorptive properties may be further explained by examining the pore size distribution plots and the BJH pore values. The materials prepared by the DT method seemed to display mainly unimodal pore size distributions in the mesoporous range of 97 Å for the 0.5 wt.% loading (Fig. 3C). An increase in the Pt loading to 1 and 2 wt.% is accompanied by slight decrease in the pore values and appears to remain invariant at around 78 Å. The differences in porosities certainly affects amount of adsorbate adsorbed and, the resultant surface area calculated. The incorporation of the surfactant capped Pt appears to have a minimal effect on the surface area irrespective of the Pt loading. The pore sizes are centered around 78 Å which is within range to that of bare titania (75 Å) suggesting that the surfactant capped Pt may be anchored in the interstitial cavities and thus non-influential on the diffusion of gas molecules to access the pores thus resulting in similar surface areas [47]. An increase in Pt loading up from 0.5 to 1 and 2% results in surface areas around 74.4, 68.7, and 89.4 m^2/g respectively. It is interesting to note that the titania crystallite sizes in surfactant based materials are maintained around 10 nm which might have an influence on the narrow range in surface areas. A summary of the textural properties, including specific surface area and BJH pore diameter obtained from nitrogen adsorption–desorption analysis are shown in Table 2.

The choice of synthetic method influences the resultant textural properties, most especially the average pore dimensions of the metal–oxide materials as observed in the surfactant free control experiments. The pore size in bare titania is centered at around 76 Å, however, the introduction of Pt species by the DX method seems to have a pronounced impact on resultant pore size distribution as shown in Fig. 3D. The pores average over a broad mesoporous range and appear to be centered around 100, 75, and 35 Å for the 0.5, 1, and 2 wt.% loading respectively. Bare titania exhibited a surface area of 65 m^2/g similar to that of the Pt-TOAB based materials thus supporting the argument that Pt species reside in the interstitial cavities. The addition of 0.5 wt.% Pt by the DX method results in a reduction in the surface area to 42.6 m^2/g. suggesting agglomeration of titania particles that minimizes access of adsorbate molecules to the pores. This is supported by the larger

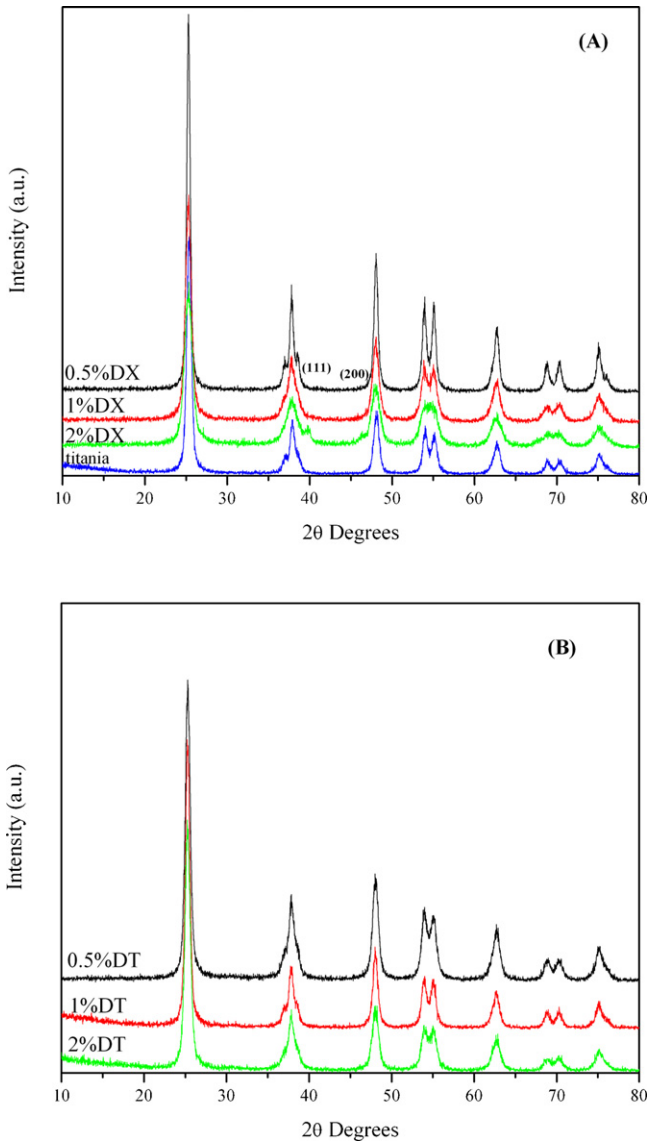

Fig. 2. Powder X-ray diffraction patterns of Pt–TiO_2 photocatalysts synthesized by (A) incorporating preformed Pt capped TOAB (DT method) into the synthesis sol, and (B) direct infusion of H_2PtCl_6 (DX method) with different Pt wt.% loadings of 0.5, 1, and 2 wt% followed by reduction of the Pt oxides at 450 °C under H_2 flow.

crystallite sizes of titania (14.7 nm) achieved for DX0.5. However, an increase in the Pt loading to 1 wt.% results in the narrowing of the pores to around 75 Å. It is likely that as the pores are narrowed, the access to the interstitial cavities is enhanced and thus facilitating an increase in surface area to 96.7 m^2/g. At this optimum loading, the dispersion of the smaller Pt (6.4 nm) is improved. A further increase in Pt loading to 2 wt.% is favorable for the enhancement of the surface area to 167 m^2/g.

The effective bandgap energies of the Pt–TiO_2 oxide materials were estimated by using UV–vis diffuse reflectance spectra transformed into Kubelka–Munk function *versus* light energy plots. Diffuse reflectance spectra (not shown) of titania demonstrate that the absorption edge achieved at ~420 nm and strong absorption by 300 nm is attributed to the excitation of electrons from the valence band to the conduction band of titania suggesting that the titania is octahedrally coordinated. The DRS spectra was converted to the linear correlation between $[F(R)h\nu]^2$ and the band gap energy *via* the Kubelka–Munk function (Tauc plot) as shown in Fig. 4. The effect of the varying the Pt content on the absorption was investigated. The

Table 1
XPS results illustrating percentage estimates of the major species of Pt and the peak positions attained.

	Major species (%)			Position $4f_{7/2}$		
	Pt^0	PtO	PtO_2	Pt^0	PtO	PtO_2
DT0.5	-	-	100	–	–	75.1
DT1	–	–	100	–	–	75.1
DT2-UC	–	–	100	–	–	75.1
DT2	–	–	100	–	–	75.1
DX0.5	−6.2	–	83.8	71.1	–	75.1
DX1	31.4	–	68.6	71.1	–	75.0
DX2-UC	-	−1.0	29.0	–	73.1	75.1
DX2	−3.4	–	46.6	71.1	–	75.1

band gap is estimated around 3.23 eV for all the three loadings for the Pt–TiO_2 prepared by the DT method as displayed in Fig. 4A. This may be ascribed to the invariance in the titania crystallite size, and this result is consistent with the XRD results that indicate sizes lying within a narrow range between 10.8 and 11.9 nm. The impact of omitting the surfactant in the preparation process (DX method) is also investigated. Bare titania exhibits a band gap of 3.20 eV and loading 0.5 wt.% Pt results in agglomeration of titania to larger crystallite sizes of 14.7 nm. It is notable that DX1 demonstrates a broader absorption in the visible region compared to its competitors, which may be linked to the photocatalyst's enhanced photocatalytic performance under simulated solar conditions (discussed later). The crystallite sizes appear to contract from 14.7 to 8.5 and 6.5 nm for the 0.5, 1 and 2 wt.% Pt loadings respectively. The effective bandgap energies were established and lie between 3.06 and 3.29 eV. In general, the Pt containing samples contain some absorption in the visible region in comparison to the bare titania.

Further information regarding the structural properties of the Pt–TiO_2 materials with percentages exhibiting the highest photocatalytic performance were explored using TEM studies. The titania fringes are clearly seen in Fig. 5A. The titania crystallite size is estimated to be 13 ± 2 nm which is within range of 11.9 nm value obtained from XRD results (Table 1). However, determination of the Pt sizes varies depending on the characterization technique employed. The CO chemisorption studies indicate that the Pt–TiO_2 prepared by the DX method contains metallic Pt^0 as evidenced by the saturation peaks observed in the uptake of CO during the pulse titration. The average Pt size determined by this approach is 6.4 ± 1 nm; this is much higher than the 2.6 ± 1 nm estimated from the TEM images and such differences have been reported previously.

The analysis carried out in this work is based on Pt sizes derived from chemisorption studies. Monnier and co-workers demonstrated the superiority of chemisorption studies over XRD and TEM analyses, as a direct measure of actual site concentrations. Most evidently, larger sample sizes are used in chemisorption analysis thus minimizing assumptions, and improving the reliability of the results obtained [48]. Overall, it is imperative to characterize the surface of the photocatalysts and XPS studies are viable in providing this information.

Quantitative XPS studies were employed to determine the chemical and electronic state of surface platinum, and consequently elucidate the contribution of the oxidation state of Pt to photocatalytic activities. The surface composition was determined by XPS survey scans of the photocatalysts examined in this study over C 1s, Br 3d, Ti 2p, O 1s, and Pt 4f spectral regions, which are shown in Figs. S1 and S2 of the supplementary information. The survey scans indicate the presence of Pt, Ti, and O atoms in addition to some adventitious carbon atoms in these materials. The DT samples indicate the absence of surfactant molecules, *i.e.* Br and N atoms from TOAB or for that matter any potassium or chloride ions arising from the Pt precursor used.

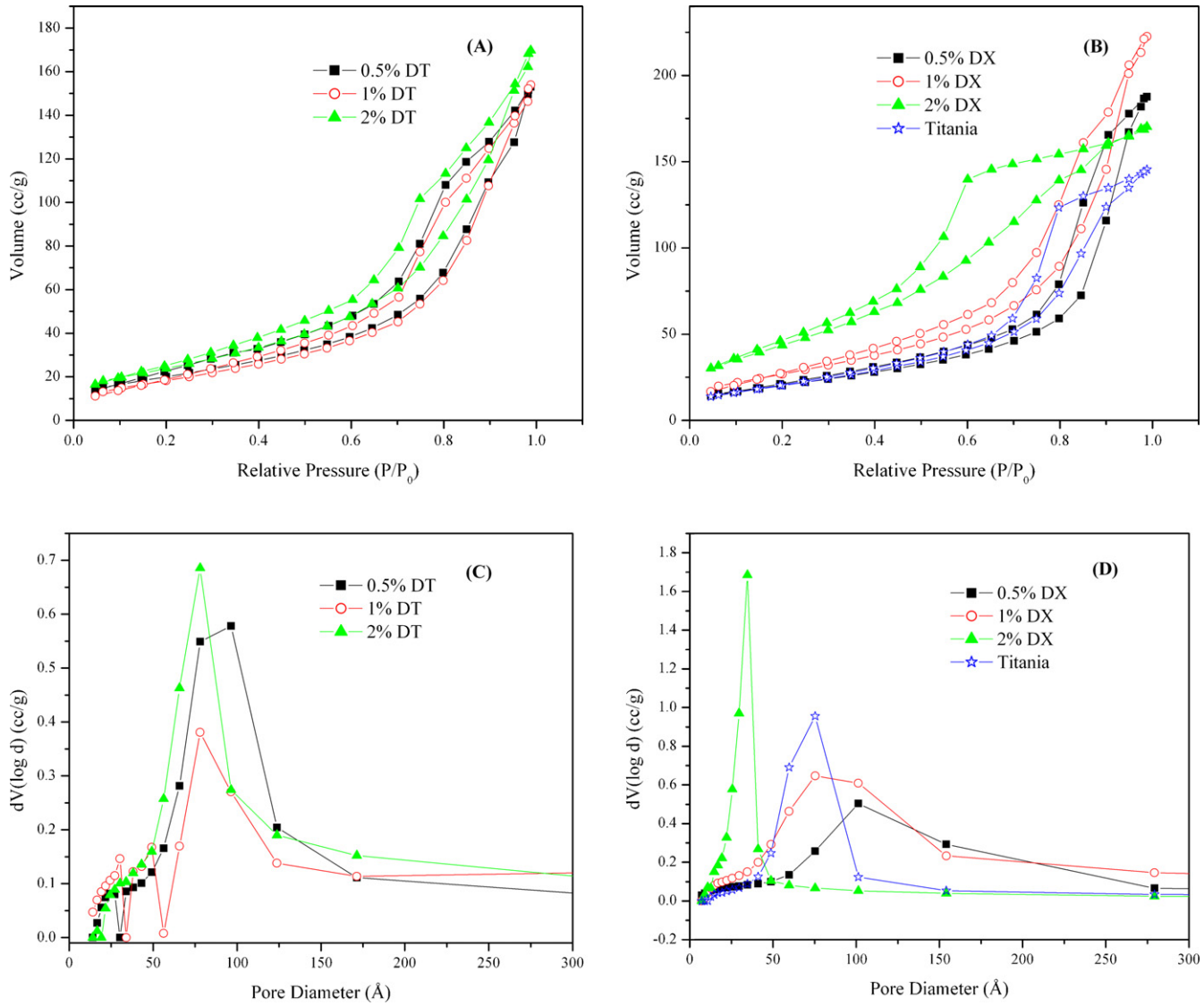

Fig. 3. (A and B) Adsorption–desorption isotherms, (C and D) pore size distribution curves comparing Pt–TiO_2 materials of different Pt wt.% loadings of 0.5, 1, and 2 wt.% prepared by the DT and the DX methods. The isotherm and pore size distribution of titania is also shown for comparison in Figs. 3B and D.

The plots in Fig. 6 display the regions due to Pt from which the amount of each oxidation state is determined. Fig. 6A shows the narrow scan of the Pt (4f) core level over uncalcined Pt–TiO_2 containing 2 wt.% Pt prepared by the DT method (DT2). The de-convoluted spectrum displays a peak around 76.0 eV corresponding to PtO_2 (Pt^{4+}) [6,36,49]. We have also performed XPS studies of DT2 sample prior to hydrogen reduction. Initially, Pt(0) nanoparticles stabilized by TOAB surfactant molecules are formed after reduction of $NaBH_4$. Known volumes of this solution were added to the sol–gel synthesis mixture and subject to hydrothermal treatment. XPS studies of the DT2 sample prior to reduction in hydrogen atmosphere (DT2-UC) indicate the presence of a peak around 75.8 eV corresponding to PtO_2. This suggests that the hydrothermal treatment provides an oxidation environment that fully oxidizes the Pt(0) nanoparticles to form PtO_2 during the hydrothermal reaction. DT2 was subjected to a reduction process under hydrogen flow in order to attain Pt^0 that is proposed to be more active for organic degradation. It is noteworthy that Pt^{4+} as PtO_2 was the only species observed.

XPS spectra of the control experiments containing surfactant free Pt species are also shown for comparison. The DX method results in Pt–TiO_2 that contains both Pt and PtO_2. The binding energies of Pt $4f_{7/2}$ for the uncalcined DX2-UC appeared *ca.* 73.2 and 76.1 eV that are attributed to PtO (Pt^{2+}) and PtO_2 (Pt^{4+}) which is consistent with published data [37,49] as shown in Fig. 6C. Thus, use of H_2PtCl_6 as the Pt precursor leads to the formation of PtO and PtO_2 during the hydrothermal reaction. The percentage content of these species is estimated at 71 and 29% respectively as indicated in Table 1.

Upon reduction treatment in hydrogen, the de-convoluted spectra of Pt 4f for DX2 result in the emergence of a peak at 71.1 eV that is attributed to Pt^0. This confirms the effectiveness of the treatment under H_2 flow as pertinent to reduce Pt^{2+} to obtain Pt^0 (62.4%) for the DX2 sample. However, this step appears insufficient in fully reducing all the Pt species to its metallic state as Pt particles are fairly susceptible to interaction with chemisorbed oxygen [49,50] to form PtO_2 (37.6%). A similar scenario is observed by other investigators whereby 100% Pt^0 is challenging to achieve [5,22,36,37,49,51]. Lee and Choi also determined that Pt_{ox} species were persistent even in the presence of electron-rich conditions [38]. Table 1 indicates the percentages of the Pt species determined by XPS studies.

In summary, the XPS suggests the presence of PtO_2/TiO_2 in the DT samples after hydrothermal treatment and after reduction (in

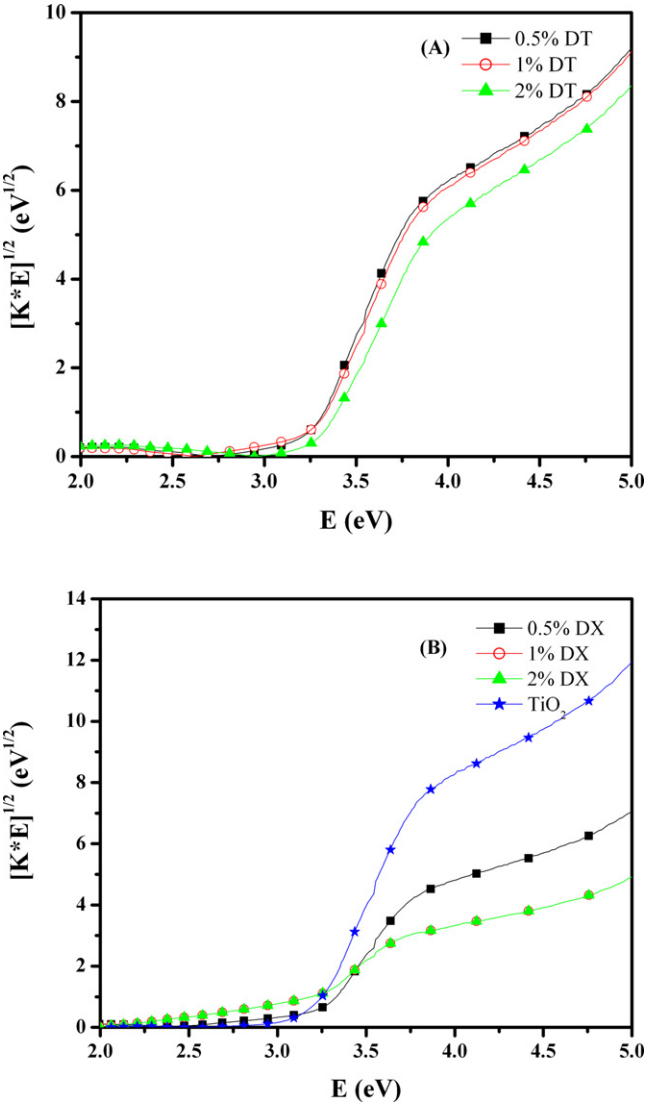

Fig. 4. Tauc plots of transformed Kubelka–Munk function *versus* light energy used to estimate the band gap energies of Pt–TiO_2 prepared by (A) DT and (B) DX methods.

hydrogen) of the hydrothermally prepared samples. In the case of the samples prepared by DX method, XPS results suggest the presence of $PtO/PtO_2/TiO_2$ after hydrothermal treatment. Reduction of the hydrothermally prepared DX samples leads to formation of $Pt/PtO_2/TiO_2$.

The hydrothermally prepared DX2 sample was subject to calcination in air at 500 °C and XPS study of this sample indicated the presence of PtO and PtO_2 with 67.5 and 32.5% respectively as indicated in Table S1. The as-synthesized DX (labeled as DX2-UC) as discussed previously showed 71.0 and 29.0% of PtO and PtO_2. Calcination in air seems to only marginally oxidize Pt^{2+} to Pt^{4+} as depicted by the spectra in Fig. S3. These results also indicate that H_2 reduction is necessary to induce the formation of Pt^0 as revealed by DX0.5, 1 and 2 wt.% that exhibit 16.2, 31.4, and 53.4% of Pt (Table 1). The increase in Pt^0 is probably due to the fact that more Pt^{n+} species are available for reduction at higher loadings. PtO_2 is still predominant at lower loadings even after completion of the H_2 reduction (DX 0.5 and DX 1). Pt^0 only is unattainable as observed by several authors in the literature, and it appears that Pt_{ox} is inevitable due to the paramount stability of the latter species. Contrary to reports, reduction under H_2 flow is insufficient in ensuring the formation of Pt^0 only [49]. This is a notion that spans the breadth of investigations with claims purporting the attainment of materials of purely Pt^0 without compelling evidence from XPS studies and clearly this study underlines the need for surface characterization. The XPS studies thus verify the conditions pertinent for achieving the desired oxidation state and the subsequent remarks assist to provide clarity on the overriding factors responsible for organic degradation.

3.3. Photocatalytic activities

The results from nitrogen adsorption, powder XRD, XPS, and photocatalytic studies are displayed in Table 2. The performance of the photocatalysts was evaluated by using Total Organic Carbon (TOC) analysis and the efficiencies are calculated as a percentage degradation of phenol after simulated solar irradiation.

The bare titania exhibited an initial (30 min) photocatalytic efficiency of 26% (based on TOC) that gradually improved to 92% after 2 h. The activity may be attributed to a range of factors such as crystallinity, surface area, and small crystallite size of titania (8.6 nm). Platinized titania was prepared to investigate the role of oxidation state on the photocatalytic efficiencies. Most literature investigations illustrate the presence of the metal species in two or more oxidation states. The motivation of this work is to discern the role of each state considering the ambiguity in the literature regarding Pt_{ox} species for phenol degradation. We are able to demonstrate that the oxidation state of choice can be achieved by synthetic colloidal methods, and in our case, PtO_2 only was realized.

Of the templated materials prepared, DT0.5 exhibits an activity 21% comparable to that of its counterparts, and this improves to 80% after 2 h of simulated solar irradiation. An increase in the Pt loading to 1 wt.% (DT1) and 2 wt.% (DT2) results in a loss in degradation to 61 and 51% respectively. This difference in activity may be attributed to accumulation of platinum species that shorten the average distance between trap states within a particle and present more recombination centers for photogenerated charge carriers [6]. These efficiencies are less than those achieved using titania in the same duration of irradiation affirming the possibility of PtO_2 serving as recombination centers especially in the later stages of the degradation of phenol under simulated solar conditions. Considering the photocatalytic reactions are substrate specific, this charge recombination is mild at low loadings *i.e.* 0.5 wt. %, compared to the complete inactivity exhibited by Pt_{ox}/TiO_2 reported for other substrates such as TCE [38]. Overall, the degradation of phenol is lower in the PtO_2/TiO_2 catalysts suggesting that the presence of PtO_2 is unfavorable to the photocatalytic activity under our experimental conditions.

The DX series, however, exhibits enhanced photocatalytic activities within the first hour of irradiation. DX0.5 contains 21.5% Pt^0 and exhibits an activity of 47% that increases to 57% when the loading is increased to an optimum of 1 wt.% and Pt^0 content of 30.4%. The activity drops off to 36% when the loading is increased to 2 wt.% and containing 62.4% of Pt^0. Since we have established that PtO_2 (Pt^{4+}), is detrimental to activity (in particular on longer irradiation times) we may deduce that an optimum amount of Pt^0 is crucial for degradation of phenol. The activity for all the photocatalysts prepared by this method is greater than 80% after 60 min of irradiation, which is superior (especially at lower irradiation times) to that of titania and PtO_2–TiO_2 under similar conditions. These results are summarized in a plot of phenol conversion *versus* time in Fig. S4, and indicate that the photocatalysts prepared by the DX method are generally more active than those prepared by the DT method.

In our study, it was surprising to note that the oxidation states of Pt (as Pt^0, PtO, or PtO_2) were invariant during the photocatalytic reaction, and the Pt speciation on fresh and spent Pt–TiO_2 were somewhat similar. The survey spectra and 4f spectral region are displayed in Fig. S5 for the photocatalysts prepared by the DT

Table 2
Textural properties of Pt–TiO_2 materials.

Material	S_{BET} [a] ($m^2\ g^{-1}$)	BJH[b] (Å)	Mean crystallite size		%PtO_2	TOC activity (%)[c]			
			TiO_2	Pt^0		30	60	90	120
Titania	65.0	75.5	8.6	–	–	26	57	80	92
DT0.5	74.4	96.7	10.6	–	100	21	40	65	80
DT1	68.7	77.7	11.9	–	100	20	36	52	69
DT2	89.4	78.1	10.8	–	100	16	29	42	51
DX0.5	42.6	100	14.7	11.4	78.5	47	83	97	97
DX1	96.7	75.1	8.5	6.4	69.6	57	94	95	95
DX2	167.0	34.8	6.5	21.1	37.6	36	89	96	98

The direct template (DT) and direct infusion (DX) methods were used for preparation of the Pt-TiO_2 photocatalysts and the subsequent values denote the Pt loading in wt. %.
[a] Surface Area was determined by applying the Brunauer–Emmett–Teller (BET) equation to the adsorption isotherm.
[b] Barrett–Joyner–Halenda (BJH) method was used to calculate the pore size distribution. Initial concentration of phenol prior to photocatalysis is 15 ppm in all instances.
[c] The values below the TOC Activity (%) indicate the reaction time in minutes of irradiation.

and DX methods respectively. The Pt in DT2-spent was determined to remain stable at 100% PtO_2, and the stability in oxidation state was evidenced by DX2-spent. The change in oxygen state of the spent DX2-C-spent sample (this hydrothermally prepared sample was calcined in air, subjected to photocatalysis experiment, and XPS studies were carried out with the spent photocatalyst) is also regarded insignificant as XPS studies indicated 67.5% PtO and 32.5% PtO_2 were achieved before and 61.7% PtO and 38.3% PtO_2 were present after the photocatalysis reaction. The results from the XPS studies are summarized in Table S1. TOC experiments of DX2-C sample indicate more than 90% phenol degradation and the high activity may be partly due to the relative low amounts of PtO_2 (32.5%) suggesting that the presence of PtO is not as detrimental to the photocatalytic activity as PtO_2.

The reasons for the variations in the photocatalytic activities of the DX series of materials were investigated, and Fig. 7 suggests an influence of the particle sizes of Pt and TiO_2. It is evident that phenol is almost completely degraded on prolonged irradiation by the DX

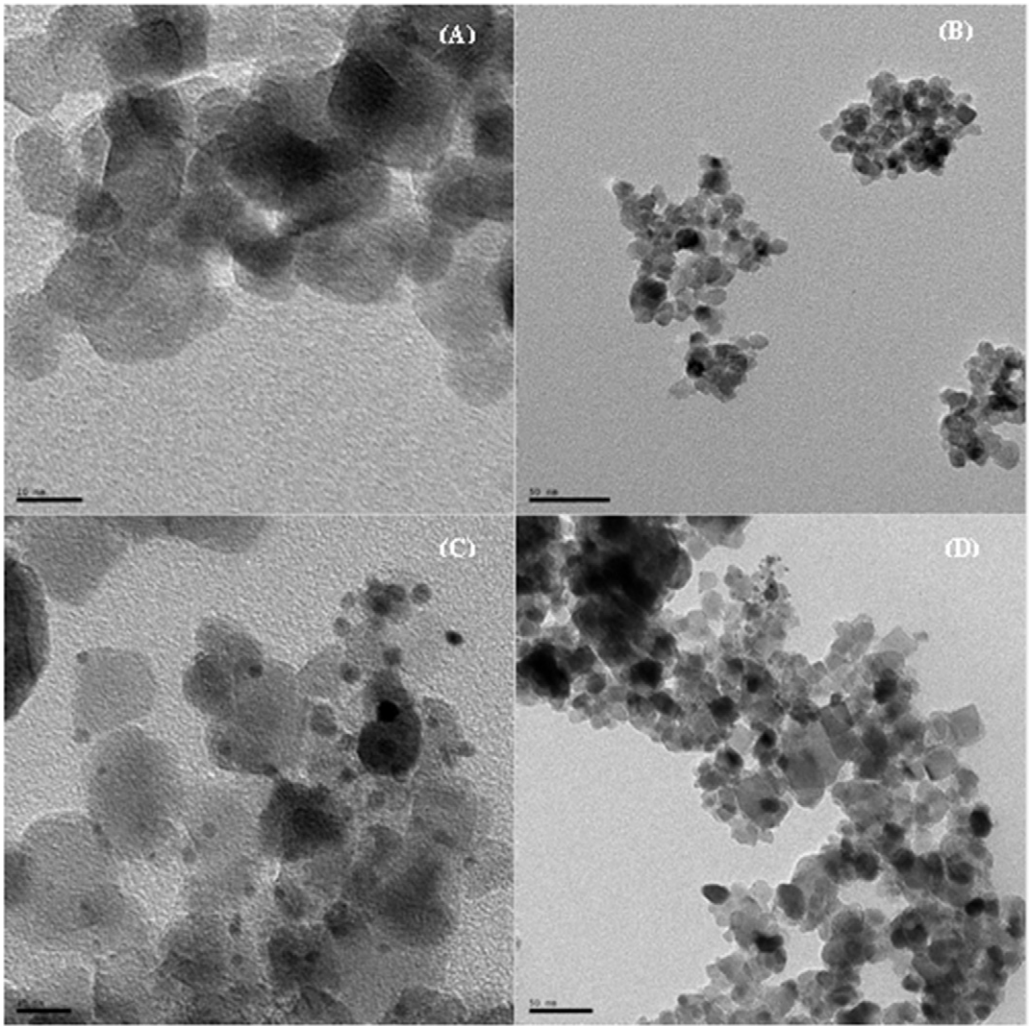

Fig. 5. TEM of Pt–TiO_2 photocatalysts with different Pt loadings of 1 wt.% synthesized by A & B) preformed Pt capped TOAB (DT method), and (C & D) direct infusion of H_2PtCl_6 (DX method). The bar scales are 10 and 50 nm from left to right.

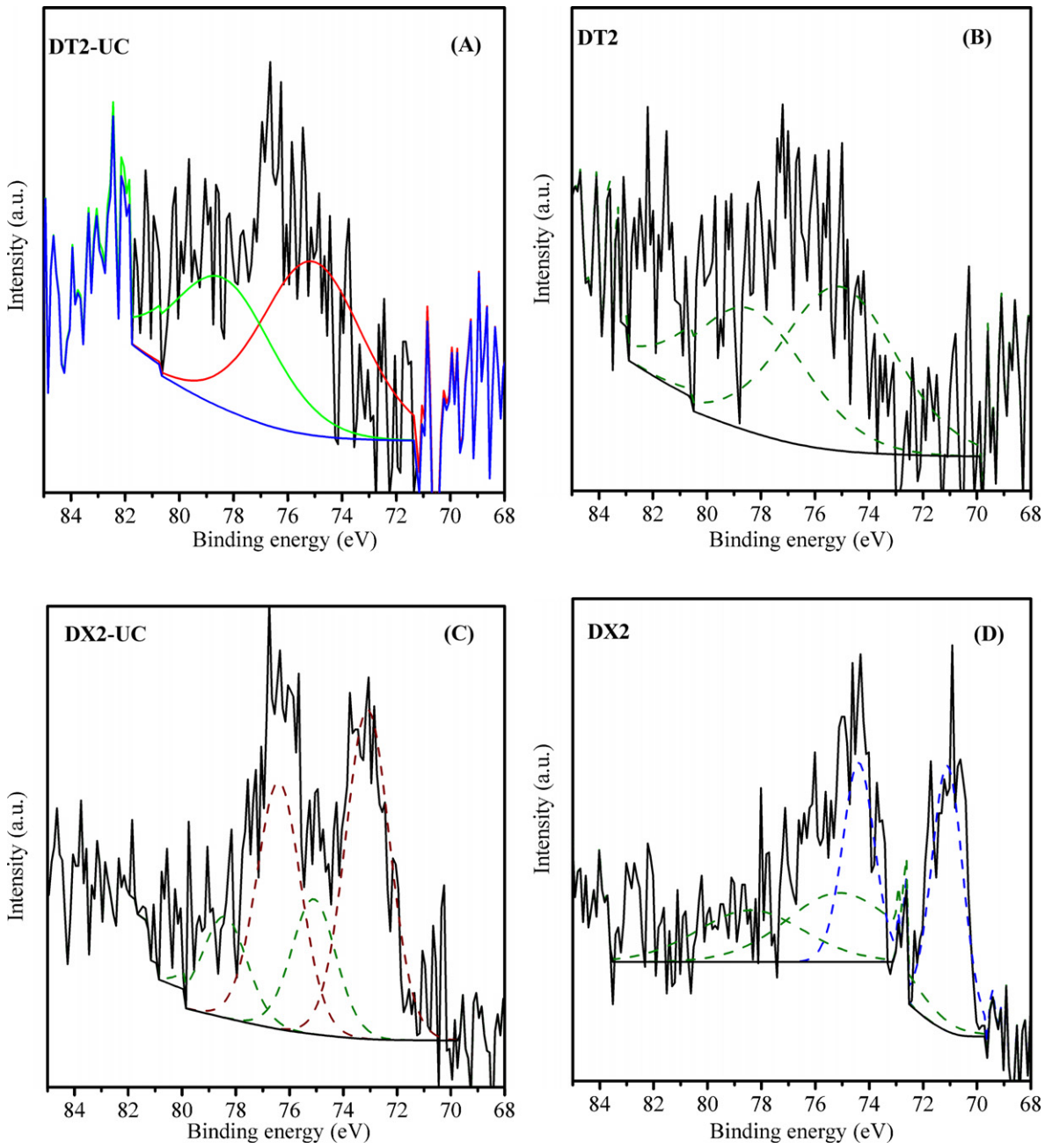

Fig. 6. High-resolution XPS spectra of Pt (4f) regions of Pt–TiO_2 with 2 wt.% of Pt, and prepared by (A,B) DT and (C,D) DX methods.

series of photocatalysts. In fact, considering similar TiO_2 sizes (6.5 and 8.5 nm) of surfactant free Pt–TiO_2 (DX), an optimum size of Pt^0 may be an overriding factor for photocatalytic degradation of phenol. This result is consistent with our previously published report in which Pt sizes in the range of 4–6.5 nm exhibited the highest activity for degradation of phenol [10]. Thus, we propose that optimal TiO_2 and small size Pt^0 crystallites are ideal for aqueous phase phenol degradation. In addition to TOC determination, we also carried out LC studies to identify the intermediates formed during the photocatalytic reactions. Some of the intermediates detected by Liquid Chromatography (LC) studies are shown in Table S2 and may include: pyrogallol (PG), hydroquinone (HQ), benzoquinone (BQ), and phenol (PhOH). LC studies indicate that DX samples are more active than DT.

We were able to control the oxidation state of Pt to 4+ using the surfactant capped preformed Pt (DT method), as well as control the TiO_2 crystallite sizes to lie between 10.6 and 11.9 nm. Since these parameters are similar, we can infer that the differences in activity are due to the fate and/or lifetime of photogenerated electrons. Our adsorption experiments indicate similar adsorption of phenol over the DT and DX series and thus the reasons for the variations in photocatalytic activity are different. The role of light intensity was investigated by conducting experiments under different light intensities in the reaction medium (91.7 mW/cm^2, 75.7 mW/cm^2, and 58.4 mW/cm^2). Under our experimental conditions of moderate to high light intensity, the phenol degradation rate appears to depend linearly on the relative light intensity thus implying a photon-limited reaction. This observation is summarized by the plot in Fig. S6 for reactions observed at 45 and 60 min under the different light intensities.

Photoluminescence experiments were conducted in order to understand this better. Representative low wt. % Pt loaded

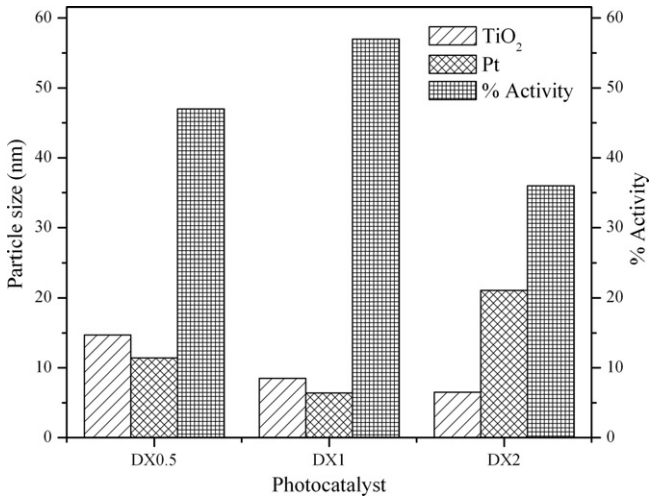

Fig. 7. Particle size effects on the photocatalytic degradation of phenol using Pt–TiO_2 prepared by the direct infusion of H_2PtCl_6 in the sol–gel route (DX method).

photocatalysts prepared by both methods were subjected to an excitation wavelength of 382 nm, and the emission spectra observed were compared to that of TiO_2 in the 400–450 nm range as shown in Fig. 8. The low wt. % loadings were chosen as they

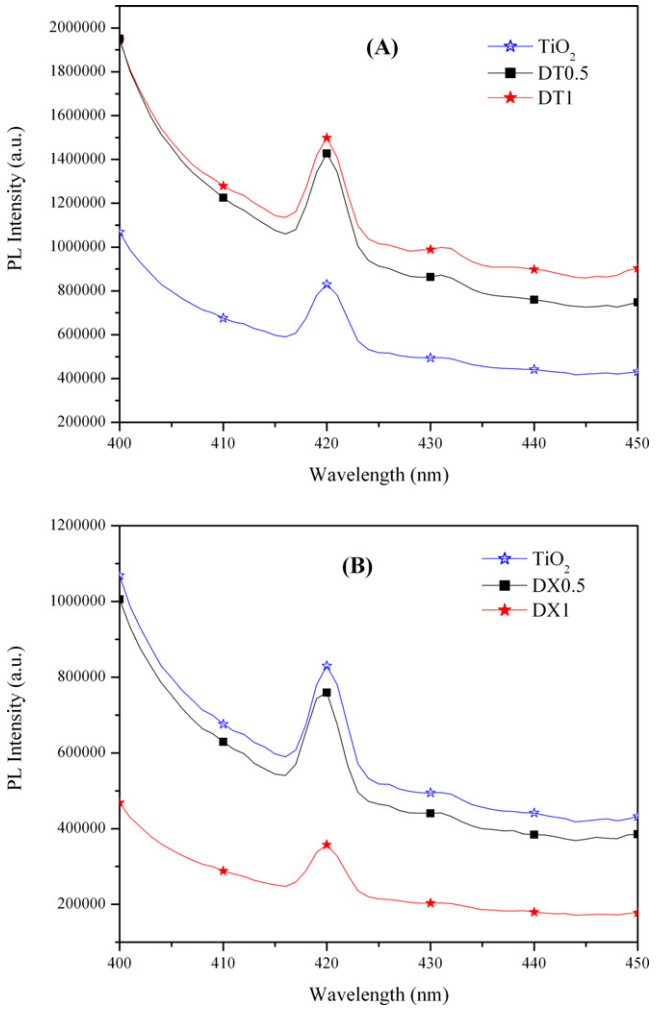

Fig. 8. Photoluminescence emission spectra of representative low loadings, 0.5 and 1 wt.% Pt–TiO_2, prepared by the DT and DX methods, and compared to TiO_2.

demonstrated the highest initial degradation rate after 60 min The peak of highest intensity was exhibited around 420 nm and is attributed to indirect $X_{1a} \rightarrow \Gamma_{1b}$ transitions of degenerate levels that are likely to have originated from strong coupling of wave functions of trapped electrons and holes with lattice phonons on the shallow trapped surface state (exciton recombination) [52]. The blue green emission observed resulted in a higher intensity spectrum for DT1, followed by DT0.5, and TiO_2 thus implicating a higher recombination rate due to higher content of PtO_2 (100%) in the DT1 photocatalyst as shown in Fig. 8A. A different trend is observed for the photocatalysts prepared by the DX method that exhibit lower recombination rates (lower PL intensity) compared to TiO_2 (Fig. 8B). Such phenomenon can be attributed to the more efficient transfer of excited electrons from the conduction band of TiO_2 to Pt owing to lesser content of PtO_2 at low loadings such as 0.5 and 1 wt.%. The presence of Pt thus results in the formation of a Schottky barrier through which electrons can migrate efficiently to adsorbed O_2 molecules and facilitate the formation of highly reactive oxidation species that result in higher degradation rates for DX prepared photocatalysts. Thus, the PL results are in general agreement with our observation that the activities of the DX series of materials are higher than that of titania and followed by the DT series.

Under N_2 purging, the photocatalytic activities of all catalysts (TiO_2, DX and DT series) were completely inhibited suggesting $O_2^{\bullet -}$ radicals are crucial for phenol degradation. In addition, experiments carried out in the dark indicate no degradation of phenol clearly suggesting that there was no catalytic contribution observed from the Pt surface as the phenol concentration was maintained around the original 15 ppm for all the photocatalysts investigated. Considering that •OH radicals are believed to be the most reactive oxidative species responsible for photocatalysis, •OH trapping experiments were carried out to estimate the formation of •OH under these solar simulated experimental conditions and understand the role of Pt in scavenging electrons. During photocatalysis, excited electrons in the conduction band may be captured by dissolved oxygen molecules to produced superoxide radicals ($O_2^{\bullet -}$) that subsequently produce •OH, which oxidize adsorbed organics. Fig. S7 shows a plot of 2-hydroxyterephthalic acid *vs.* time for TiO_2, DX0.5, and DT0.5 photocatalysts. It can be seen that as the reaction progresses, the number of •OH decreases in TiO_2 and DT0.5 photocatalysts due to more charge carrier recombination and thus they produce less amounts of 2-hydroxyterephthalic acid as compared to the DX0.5 photocatalyst. It is observed that the •OH formation is maintained even after 80 min in DX0.5 implying that the Pt^0 serves as an electron sink and facilitates the transfer of electrons to the dissolved oxygen and eventually form more reactive oxidative species that degrade phenol more efficiently. Similar trends were observed for the other DT and DX series of photocatalysts. Thus, the improved electron–hole separation in DX series of photocatalysts, invoked by the presence of Pt^0, is responsible for its enhanced activity. In contrast, the DT series contains PtO_2 and these photocatalysts are not effective in minimizing electron–hole recombination.

Although the lower recombination rate is in good agreement with the higher activity for such materials, caution is advised in vindicating the influence of physicochemical properties on the electronic properties and thus the resultant photocatalytic efficiencies, which could as well be substrate specific. The synthetic procedures that determine these parameters are paramount for the development of these light active semiconductor photocatalysts.

4. Conclusions

A synthetic procedure was devised that enabled the control of the oxidation state in Pt–TiO_2 photocatalysts. Preformed platinum was attained by a phase transfer reduction method using TOAB

capping agent, and the resultant organosol (Pt-TOAB) was utilized for the preparation of the PtO_2–TiO_2. A comparison with the control photocatalysts enabled the following observations:

1. PtO_2–TiO_2 containing 100% PtO_2 (Pt^{4+}) can be synthesized by simple methods incorporating a combination of phase transfer chemistry and hydrothermal treatment using TOAB as a surfactant.
2. The platinum oxidation state (4+) as well as the particle size of titania (~11 nm) can be maintained using this method and the difference in photocatalytic activity was attributed to the Pt loading *i.e.* higher loadings enhance charge carrier recombination.
3. The surfactant free photocatalysts (control) of similar titania sizes contain Pt^0 whose crystallite size appears to be overriding factor influencing phenol degradation and the highest activity is demonstrated at an optimum Pt loading of 1 wt.%.
4. The activity follows the trend, $Pt^0/PtO_2/TiO_2 > TiO_2 > PtO_2/TiO_2$ and therefore PtO_2 serves as a mild recombination center for photogenerated charge carriers rather than demonstrating total inactivity.

Acknowledgements

We extend sincere gratitude to NSF-CHE-0619190, NSF-CHE-0722632, NSF-CHE-0840507, NSF-EPS-0903804, DE-FG02-08ER64624, Sigma Xi-G20101015154662, SD NASA EPSCoR NNX12AB17G and the State of South Dakota for funding this project. We also thank Central Microscopy Research Facility, University of Iowa for XPS studies, Dr. Cuikun Lin for assistance with TEM studies, and the International Precious Metals Institute (IPMI) Student Award 2010.

Appendix A. Supplementary data

Supplementary data associated with this article can be found, in the online version, at http://dx.doi.org/10.1016/j.apcatb.2013.01.062.

References

[1] V. Subramanian, E. Wolf, P.V. Kamat, The Journal of Physical Chemistry B 105 (2001) 11439–11446.
[2] P.V. Kamat, The Journal of Physical Chemistry B 106 (2002) 7729–7744.
[3] P.V. Kamat, The Journal of Physical Chemistry C 111 (2007) 2834–2860.
[4] M. Jakob, H. Levanon, P.V. Kamat, Nano Letters 3 (2003) 353–358.
[5] W.Y. Teoh, L. Mädler, R. Amal, Journal of Catalysis 251 (2007) 271–280.
[6] F.B. Li, X.Z. Li, Chemosphere 48 (2002) 1103–1111.
[7] H. Härelind Ingelsten, J.-C. Béziat, K. Bergkvist, A. Palmqvist, M. Skoglundh, H. Qiuhong, L.K.L. Falk, K. Holmberg, Langmuir 18 (2002) 1811–1818.
[8] R. Zanella, S. Giorgio, C.R. Henry, C. Louis, The Journal of Physical Chemistry B 106 (2002) 7634–7642.
[9] F. Zhang, J. Chen, X. Zhang, W. Gao, R. Jin, N. Guan, Y. Li, Langmuir 20 (2004) 9329–9334.
[10] H.S. Kibombo, R.T. Koodali, The Journal of Physical Chemistry C 115 (2011) 25568–25579.
[11] M.P. Pileni, Langmuir 17 (2001) 7476–7486.
[12] J. Yang, J.Y. Lee, J.Y. Ying, Chemical Society Reviews 40 (2011) 1672–1696.
[13] C.-S. Lin, M.R. Khan, S.D. Lin, Journal of Colloid and Interface Science 299 (2006) 678–685.
[14] Y. Mizukoshi, R. Oshima, Y. Maeda, Y. Nagata, Langmuir 15 (1999) 2733–2737.
[15] G.H. Woehrle, L.O. Brown, J.E. Hutchison, Journal of the American Chemical Society 127 (2005) 2172–2183.
[16] T. Herricks, J. Chen, Y. Xia, Nano Letters 4 (2004) 2367–2371.
[17] K. Wikander, C. Petit, K. Holmberg, M.-P. Pileni, Langmuir 22 (2006) 4863–4868.
[18] E.G. Castro, R.V. Salvatierra, W.H. Schreiner, M.M. Oliveira, A.J.G. Zarbin, Chemistry of Materials 22 (2009) 360–370.
[19] K. Kimura, H. Einaga, Y. Teraoka, Catalysis Letters 139 (2010) 72–76.
[20] M. Abu Bakar, J. Ismail, C.H. Teoh, W.L. Tan, N.H.H. Abu Bakar, Journal of Nanomaterials 2008 (2008) 1–8.
[21] D.I. Gittins, F. Caruso, Angewandte Chemie International Edition 40 (2001) 3001–3004.
[22] J. Prabhuram, X. Wang, C.L. Hui, I.M. Hsing, The Journal of Physical Chemistry B 107 (2003) 11057–11064.
[23] U. Siemon, D. Bahnemann, J.J. Testa, D. Rodriguez, M.I. Litter, N. Bruno, Journal of Photochemistry and Photobiology A: Chemistry 148 (2002) 247–255.
[24] B. Sun, A.V. Vorontsov, P.G. Smirniotis, Langmuir 19 (2003) 3151–3156.
[25] D. Hufschmidt, D. Bahnemann, J.J. Testa, C.A. Emilio, M.I. Litter, Journal of Photochemistry and Photobiology A: Chemistry 148 (2002) 223–231.
[26] W.Y. Teoh, L. Mädler, D. Beydoun, S.E. Pratsinis, R. Amal, Chemical Engineering Science 60 (2005) 5852–5861.
[27] T. Sreethawong, S. Yoshikawa, International Journal of Hydrogen Energy 31 (2006) 786–796.
[28] C.A. Emilio, M.I. Litter, M. Kunst, M. Bouchard, C. Colbeau-Justin, Langmuir 22 (2006) 3606–3613.
[29] F. Denny, J. Scott, K. Chiang, W.Y. Teoh, R. Amal, Journal of Molecular Catalysis A: Chemical 263 (2007) 93–102.
[30] I. Pastoriza-Santos, L.M. Liz-Marzán, Langmuir 18 (2002) 2888–2894.
[31] B.L. Cushing, V.L. Kolesnichenko, C.J. O'Connor, Chemical Reviews 104 (2004) 3893–3946.
[32] M. Harada, K. Okamoto, M. Terazima, Langmuir 22 (2006) 9142–9149.
[33] Y. Zhang, D. Kang, C. Saquing, M. Aindow, C. Erkey, Industrial & Engineering Chemistry Research 44 (2005) 4161–4164.
[34] F. Bernardi, M.C.M. Alves, J. Morais, The Journal of Physical Chemistry C 114 (2010) 21434–21438.
[35] A.V. Vorontsov, E.N. Savinov, J. Zhensheng, Journal of Photochemistry and Photobiology A: Chemistry 125 (1999) 113–117.
[36] C.-H. Huang, I.K. Wang, Y.-M. Lin, Y.-H. Tseng, C.-M. Lu, Journal of Molecular Catalysis A: Chemical 316 (2010) 163–170.
[37] H. Wang, Z. Wu, Y. Liu, Y. Wang, Chemosphere 74 (2009) 773–778.
[38] J. Lee, W. Choi, The Journal of Physical Chemistry B 109 (2005) 7399–7406.
[39] B. Sun, P.G. Smirniotis, P. Boolchand, Langmuir 21 (2005) 11397–11403.
[40] D. Xu, Z. Liu, H. Yang, Q. Liu, J. Zhang, J. Fang, S. Zou, K. Sun, Angewandte Chemie International Edition 48 (2009) 4217–4221.
[41] M. Brust, M. Walker, D. Bethell, D.J. Schiffrin, R. Whyman, Journal of the Chemical Society, Chemical Communications (1994) 801–802.
[42] W. Cheng, E. Wang, The Journal of Physical Chemistry B 108 (2003) 24–26.
[43] T. Teranishi, M. Hosoe, T. Tanaka, M. Miyake, The Journal of Physical Chemistry B 103 (1999) 3818–3827.
[44] D.L. Swihart, W.R. Mason, Inorganic Chemistry 9 (1970) 1749–1757.
[45] M. Kruk, M. Jaroniec, Chemistry of Materials 13 (2001) 3169–3183.
[46] S.S. Lowell J.E., M.A. Thomas, M. Thommes, Characterization of Porous Solids and Powders: Surface Area, Pore Size and Density, Academic Press Inc, San Diego, 1990.
[47] B.M. Reddy, B. Manohar, E.P. Reddy, Langmuir 9 (1993) 1781–1785.
[48] K. Punyawudho, D.A. Blom, J.W. Van Zee, J.R. Monnier, Electrochimica Acta 55 (2010) 5349–5356.
[49] B. Ohtani, K. Iwai, S.-i. Nishimoto, S. Sato, The Journal of Physical Chemistry B 101 (1997) 3349–3359.
[50] T. Sano, N. Negishi, K. Uchino, J. Tanaka, S. Matsuzawa, K. Takeuchi, Journal of Photochemistry and Photobiology A: Chemistry 160 (2003) 93–98.
[51] S. Kim, S.-J. Hwang, W. Choi, The Journal of Physical Chemistry B 109 (2005) 24260–24267.
[52] P.M. Kumar, S. Badrinarayanan, M. Sastry, Thin Solid Films 358 (2000) 122–130.